Layer-by-Layer Single-crystal Two-dimensional Material Growth by Geometric Confinement

By

Doyoon Lee

B.S., Material Science and Engineering
Hongik University, 2016

M.S., Material Science and Engineering
Hongik University, 2019

Submitted to the Department of Mechanical Engineering
in Partial Fulfillment of the Requirements for the Degree of

MASTER OF SCIENCE IN MECHANICAL ENGINEERING

at the

MASSACHUSETTS INSTITUTE OF TECHNOLOGY

JUNE 2023

Authored by: Doyoon Lee
Department of Mechanical Engineering
May 12, 2023

Certified by: Jeehwan Kim
Associate Professor of Mechanical Engineering
Thesis Supervisor

Accepted by: Nicolas Hadjiconstantinou
Professor of Mechanical Engineering
Chairman, Department Committee on Graduate Theses

Layer-by-Layer Single-crystal Two-dimensional Material Growth by Geometric Confinement

by

Doyoon Lee

Submitted to the Department of Mechanical Engineering on May 12, 2023
in partial fulfillment of the requirements for the degree of
Master of Science in Mechanical Engineering

Abstract

Two-dimensional (2D) transition metal dichalcogenides (TMDs) and their heterostructures have been widely studied for next-generation electronics. However, the following critical challenges have hindered them from their commercialization: 1) precise layer control during their growth, 2) maintaining single crystallinity at wafer-scale, and 3) inevitable transfer-process to fabricate heterostructure for various next-generation applications such as spintronics, valleytronics, and optoelectronics.

This thesis introduces a confined-growth technique that can overcome the aforementioned hurdles simultaneously by introducing a geometric SiO_2 mask that has growth selectivity from the underlying substrate. As micrometer-scale SiO_2 trenches reduce the growth duration substantially, single-domain WSe_2 and MoS_2 arrays are obtained on an arbitrary substrate at wafer-scale by filling the trenches before the second layer of nuclei is introduced, thus enabling layer-by-layer growth without requiring epitaxial seeding.

In addition, subsequent MoS_2 growth on the WSe_2 arrays yields MoS_2/WSe_2 heterostructures. Therefore, we for the first time demonstrate single-domain TMDs arrays and their heterostructures at wafer-scale with controllable thickness, which of performances are comparable to that fabricated from TMDs flake. This confined-growth technique not only can overcome key obstacles of 2D materials, but also provide a platform with great potential for next-generation 2D-material-based applications.

Thesis Supervisor: Jeehwan Kim

Title: Associate Professor of Mechanical Engineering

Acknowledgements

First and foremost, I would like to thank my advisor, Professor Jeehwan Kim, for mentoring and fully supporting me during my time at MIT. His enthusiasm for research and numerous creative ideas to overcome key challenges in academy and industry and to change the world always inspired and motivated me. I also have learned how important it is to have a positive attitude and mindset not only to research but also to daily life to become an influential researcher and human being. I believe what I learned from him will be a strong basis for my future career.

I would also like to thank the members of Professor Kim's group. It has been a great chance to learn tremendous knowledge and research skills from each group member with a different background. I specially thank Prof. Sang-Hoon Bae who was my first mentor when I joined the group and has kept teaching and motivating me. Many thanks to Dr. Hyunseok Kim, Dr. Kiseok Kim and Prof. Hanwool Yeon for advising, guiding, and working closely with me. I would not have had progress and achievement without the help from the group members.

Lastly, I would like to express my gratitude to my family. Thank my wife, Yesol Lee, for giving me so much love and support over the past 8 years. I am grateful to my mother and father for raising me and supporting me unconditionally until today. Also, thank my mother-in-law and father-in-law for their full support so far. I would not be here at MIT without you.

Contents

1. Introduction
1.1. Background ····· 9
1.1.1.Two-dimensional materials ····· 9
1.1.2.Two-dimensional heterostructure ····· 9
1.1.3.Challenges of two-dimensional materials ····· 10
1.2. Outline ····· 10
2. Experiments and results
2.1. Selective confined growth of transition metal dichalcogenides ····· 11
2.2. Density function theory (DFT) calculation ····· 12
2.3. Optimization of growth condition ····· 13
2.4. Material characterization ····· 15
2.5. Device performances ····· 18
3. Conclusions ····· 22
Appendix A: Experimental methods ····· 24
Appendix B: Theoretical calculations ····· 28
References ····· 31

Chapter 1

Introduction

1.1 Background

1.1.1 Two-dimensional materials

Two-dimensional (2D) materials are an emerging class of materials with fascinating electronic, optical, mechanical, and chemical properties that are distinct from their bulk counterparts. These materials are characterized by their ultra-thin thickness, typically just a few atomic layers thick, and their high surface-to-volume ratio. This unique morphology gives rise to a range of remarkable properties, such as high electron mobility, excellent mechanical strength, and high transparency. Two-dimensional materials have the potential to revolutionize various fields, including electronics, optoelectronics, energy, and biomedical engineering, among others. Graphene, the first 2D material to be discovered, has received considerable attention since its discovery in 2004[1], but a plethora of other 2D materials, including transition metal dichalcogenides (TMDs), black phosphorus, and hexagonal boron nitride (hBN), have since been discovered[2]. As research into 2D materials continues to grow, their unique properties are likely to unlock new scientific discoveries and technological innovations.

1.1.2 Two-dimensional heterostructure

2D heterostructures, consisting of different 2D materials stacked together in a precisely controlled manner, have attracted significant attention in recent years due to their unique properties and potential applications[3,4]. By combining the distinct properties of different 2D materials, such as graphene, TMDs, and hBN, into a single structure, new and enhanced properties can emerge, leading to the development of novel devices and applications.

One of the most promising applications of 2D heterostructures is in the field of electronics. By using 2D materials with different bandgaps, for example, it is possible to create efficient transistors with high on-off ratios and low power consumption[5]. Additionally, the use of 2D heterostructures in optoelectronics has shown great potential, with applications in solar cells, photodetectors, and light-emitting diodes. In addition, state-of-the-art applications include valleytronics and spintronics[6-10].

Beyond electronics, 2D heterostructures have also shown promise in catalysis, energy storage, and sensing applications. The high surface-to-volume ratio of 2D materials makes them excellent candidates for catalytic reactions, and by combining different 2D materials in a heterostructure, it is possible to create efficient catalysts with enhanced activity and selectivity[11]. Similarly, 2D heterostructures have shown great promise in energy storage applications[12], with the potential to create ultrathin and high-capacity batteries and supercapacitors.

Overall, 2D heterostructures represent a promising new class of materials with a range of potential applications. As research in this area continues to progress, we can expect to see new and exciting developments in electronics, optoelectronics, catalysis, energy storage, and sensing, among other fields.

1.1.3 Challenges of two-dimensional materials

Even though 2D transition metal dichalcogenides (TMDs) and their heterostructures are promising for next-generation device applications, so far, limited scalability has been challenging for the integration of 2D heterostructures onto industrial platforms. The most common method to fabricate 2D heterostructure is mechanical exfoliation, transfer and stacking of 2D flakes, which requires trial-and-error process with long assembly time and leads to limited size of the structure up to 100 micrometers due to originally small size of the 2D flakes.

Recently, an 'epitaxial' growth method has been reported that can obtain single-crystalline monolayer TMDs on sapphire substrate to address scalability issue[13]. However, there are still critical challenges: 1) lack of layer-by-layer growth of single-domain TMDs to grow 2D heterostructure at large-scale, and 2) inevitable transfer process of 2D materials onto Si substrate for device fabrication.

A 'non-epitaxial' growth method has also been reported using laser irradiation on nucleation spots to grow single-domain TMDs arrays[14]. However, this method results in undesirable damage in TMDs. In addition, lateral heterostructures form preferably at the defect sites when a vertical growth of the second heterolayer is attempted.

1.2 Outline

Here, we demonstrate 1) non-epitaxial direct growth to obtain single-domain TMDs at wafer-scale on Si substrate coated with an amorphous oxide layer for commercialization, and 2) single-domain heterostructure TMDs at wafer-scale by layer-by-layer growth[15].

Our strategy to achieve these is patterning a-SiO_2 mask that has growth selectivity from the underlying substrate, where TMDs are preferably grown as a single-domain on the exposed substrate area of less than a few micrometers. We performed density function theory (DFT) calculation to verify the idea.

We then optimized experimental parameters such as chemical vapor deposition (CVD) growth conditions and mask dimension to obtain single-domain TMDs arrays. After achieving single-domain WSe_2 and MoS_2 arrays and their heterostructure at wafer-scale, we characterized the TMDs arrays using Raman spectroscopy, photoluminescence (PL), scanning electron microscopy (SEM), high-resolution transmission electron microscopy (HRTEM), high-angle annular dark field scanning transmission electron microscopy (HAADF-STEM), X-ray photoelectron spectroscopy (XPS) to confirm material quality. We also fabricated field effect transistor (FET) arrays and measured electrical performances which were comparable to that fabricated by TMDs flake.

Chapter 2

Experiments and results

2.1 Selective confined growth of transition metal dichalcogenides

Figure 1 shows the conventional transition metal dichalcogenides (TMD) growth method and our non-epitaxial confined growth method. In conventional growth method, the first sets of nuclei are formed in random orientation on the substrate, and they laterally grow to be merged, forming grain boundaries. In addition, the second sets of nuclei are introduced if without precise kinetic control before the first layer is fully merged to form continuous film (Figure 1a). The merged film becomes polycrystalline layer with irregular thickness due to the random orientation of initial nuclei and uncontrollable nucleation, degrading the intrinsic material properties.

To address the above issues, we patterned a few micrometers size of a-SiO_2 mask on *c*-Al_2O_3 or a-HfO_2-deposited Si/SiO_2 substrate. As a-SiO_2 has lower nucleation density compared to the substrate, TMDs are selectively grown inside a-SiO_2 trench. In addition, the trench size is small enough to allow one single-domain nuclei in each trench, which later grows and fills up the entire trench. The resulting TMDs layer is single-domain monolayer with no grain boundary (Figure 1b). Single-domain heterostructure was also achieved by consecutively growing another TMDs on the first layer (Figure 1c).

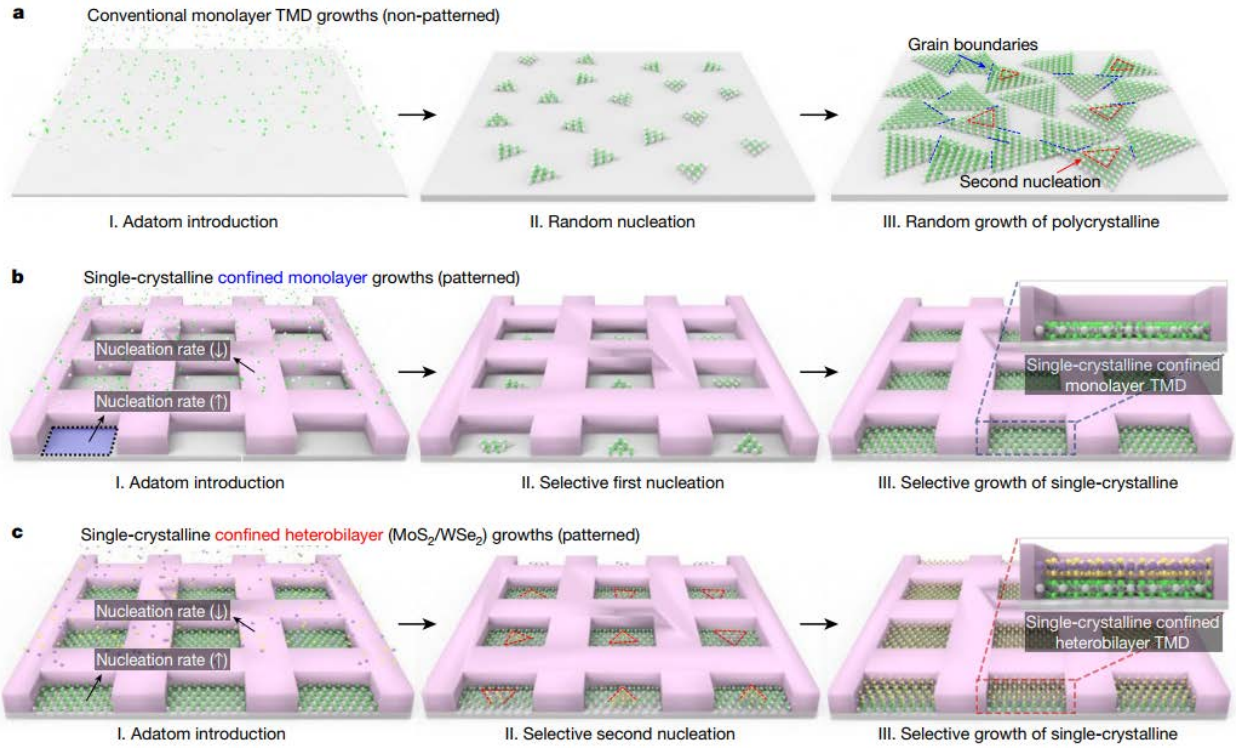

Figure 1. Schematic and synthesis mechanism of selective single-domain TMD arrays. a. Schematic of the general process by which TMDs are grown. Stage I shows the same chance of nucleation across the entire area. **b.** Schematic of the selective single-domain synthesis strategy to address the limitations of conventional TMD growth. **c.** Single-domain MoS_2/WSe_2 heterostructures by confined growth of a second MoS_2 layer.

2.2 Density function theory (DFT) calculation

We performed density function theory (DFT) calculations to confirm growth selectivity between a-SiO_2 mask and substrate. Figure 2 shows calculated binding energies of WO_3, Se, and WSe_2 cluster, which are precursors and product for WSe_2 growth, on *c*-Al_2O_3, a-HfO_2 and a-SiO_2. The precursors and product have stronger binding energies with *c*-Al_2O_3, a-HfO_2 compared to a-SiO_2, indicating that they preferably bind to the substrates rather than a-SiO_2 mask and leading to selective WSe_2 growth.Atomic force microscopy (AFM) images in figure 3 shows simultaneous growth results of WSe_2 on *c*-Al_2O_3, a-HfO_2 and a-SiO_2 under the same chemical vapor deposition (CVD) condition and confirms their growth selectivity.

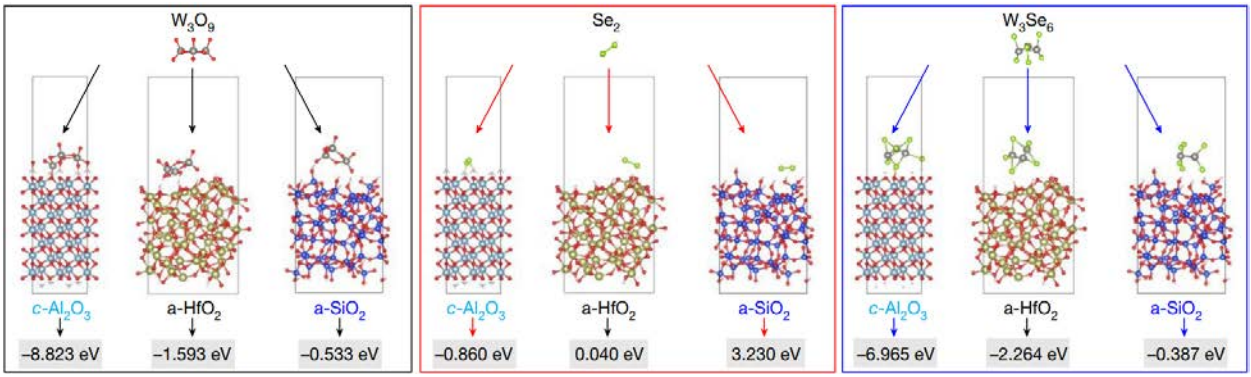

Figure 2. Density function theory (DFT) calculation. The binding energies of W_3O_9 (black box), Se_2 (red box) and W_3Se_6 (blue box) cluster on c-Al_2O_3, a-HfO_2 and a-SiO_2 substrates.

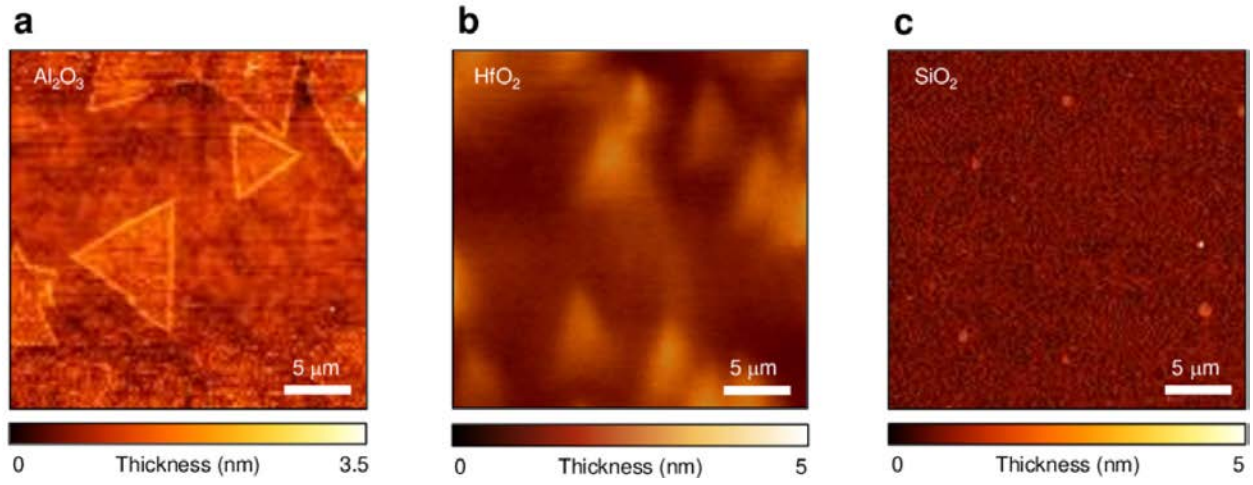

Figure 3. Growth selectivity on *c*-Al_2O_3, a-HfO_2 and a-SiO_2 substrates. a–c. AFM images of WSe_2 grown on *c*-Al_2O_3 (a), a-HfO_2 (b), and a-SiO_2 (c) under the same CVD process conditions. WSe_2 only nucleates on the *c*-Al_2O_3 and a-HfO_2 instead of a-SiO_2 during 20 min of growth duration. This led to a successful selective confined growth of WSe2 on the exposed substrate surface of the micropatterned a-SiO_2 trench arrays.

2.3 Optimization of growth condition

We determined the proper size of the a-SiO_2 trenches that allow only one single-domain WSe_2 nuclei at each trench area by measuring the lateral growth rate of the WSe_2 and incubation time for the second layer nucleation after the first set of nuclei. Figure 4 shows domain size distibutions and their scanning electron microscopy (SEM) images at different growth time with 25nm-thick and 2 μm-width trenches on *c*-Al_2O_3 substrate. The measured lateral growth rate of WSe_2 and the incubation time for the second layer of nucleation were about 0.4 μm/min and 5 min, respectively.

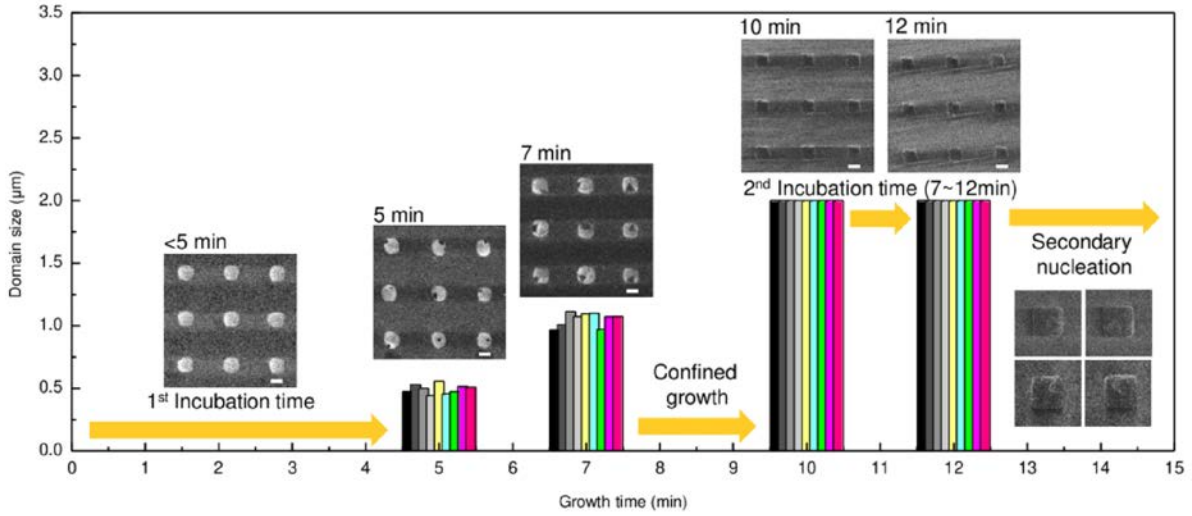

Figure 4. Lateral growth rate and secondary nucleation time for confined growth. After an incubation time of 5 min, WSe_2 was laterally grown up to 10 min, and secondary nucleation occurred after a confined monolayer was maintained for an additional 2 min. Scale bar, 2 μm.

We further investigated behavior of WSe_2 domain during the growth with different SiO_2 trench dimensions. As shown in Figure 5a, growing WSe_2 on 10 μm-width trenches longer than the incubation time introduces multiple domains in each trench (red and green boxes for multi domains and yellow boxes for single domain). The trenches with multi domains WSe_2 are eventually filled up at increased growth time and they become polycrystalline with grain boundaries (Figure 5b).

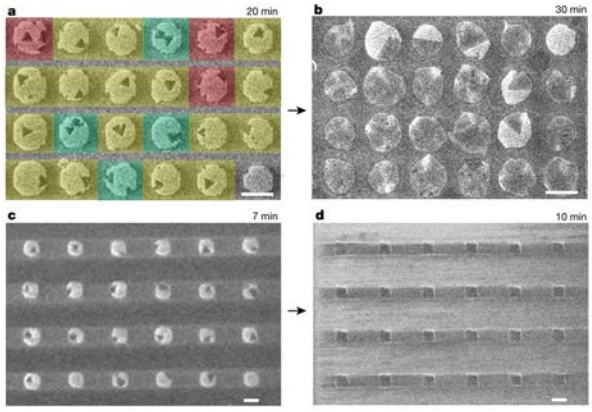

Figure 5. Selective single-domain synthesis and layer-by-layer confined growth of WSe_2. a–d. Single-domain WSe2 selectively synthesized in 10-μm (a,b) and 2-μm (c,d) sapphire pockets fabricated with a-SiO2 trenches.

On the other hand, with decreased trench width of 2 μm, only one single domain is formed in each trench regardless of whether it is homogeneous nucleation at the center of trenches or heterogeneous nucleation at the edge of trenches (Figure 5c). The single domain WSe_2 fills up the trench at increased growth time as shown in Figure 5d and we obtained single-crystalline WSe_2 array at the wafer scale.

Figure 6 statistically confirms that all trenches are filled with single domain WSe_2 across the 2-inch wafer by measuring SEM. In addition, the growth duration to fill up the trench substantially decreases from 30 min with 10 μm-width trenches to 10 min with 2 μm-width trenches, suppressing second-layer nucleation on the first layer and enabling controllable layer-by-layer growth.

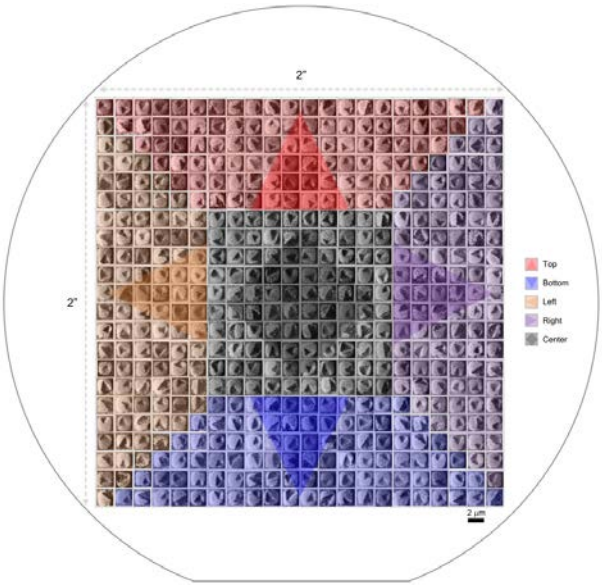

Figure 6. Statistics of WSe_2 single domains grown in 2 μm-size trench patterns. Each denoted top (red), bottom (blue), left (orange), and right (violet) region on the wafer includes 96 dies, whereas the denoted center region (black) on the wafer includes 100 dies.

The same process was performed for MoS_2 with 1 μm-width trenches on a-HfO_2 coated Si/SiO_2 substrate, indicating that the single domain confined growth can also be used for other types of TMDs not only on *c*-Al_2O_3 but also on amorphous oxide coated Si substrates for Si-based technology (Figure 7).

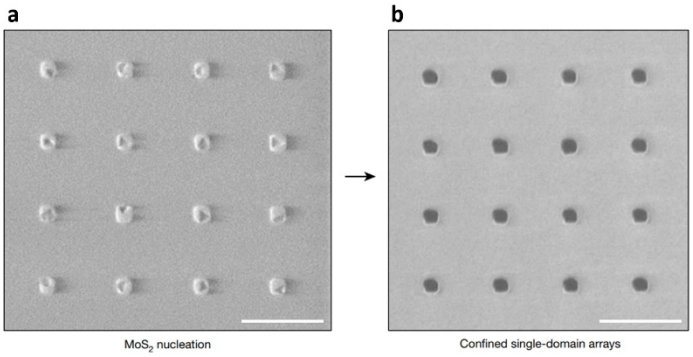

Figure 7. a,b. Single-domain MoS_2 selectively synthesized in 1-μm a-HfO_2 pockets fabricated with a-SiO_2 trenches. Scale bars, 5 μm.

SEM images and cross-sectional TEM images in Figure 8 show that the number of WSe_2 layers can be precisely controlled by increasing growth time. In addition, single-domain WSe_2/MoS_2 heterostructure with sharp van der Waals interface was also achieved by consecutively growing MoS_2 on the monolayer confined WSe_2 arrays and confirmed by high-angle annular dark field scanning transmission electron microscopy (HAADF-STEM) in Figure 8e.

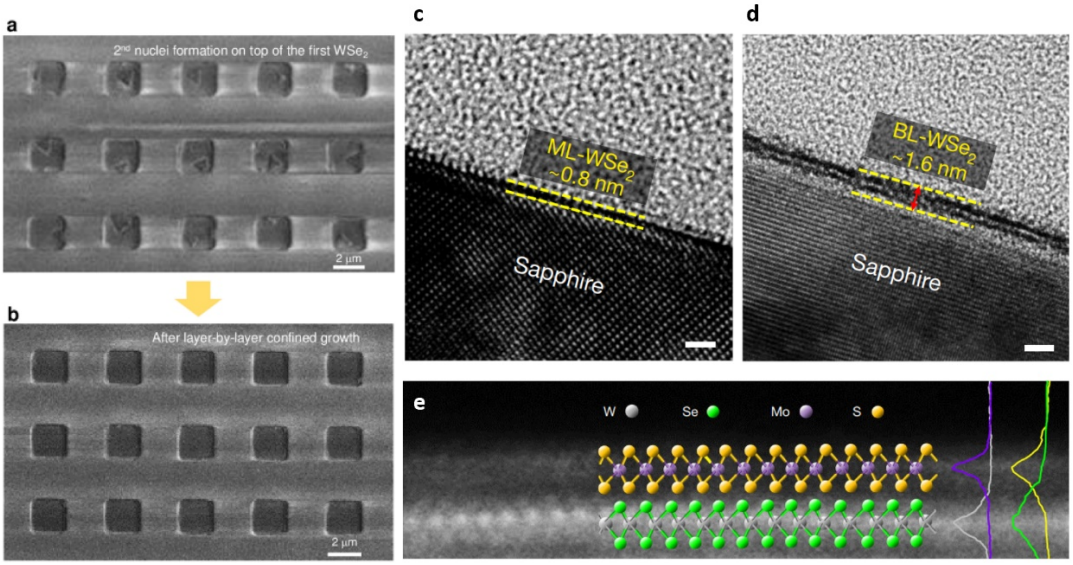

Figure 8. SEM and cross-sectional TEM images of confined ML- and BL-WSe_2 and WSe_2/MoS_2 heterostructure. a,b. SEM images of second layer nuclei on the first layer of confined WSe_2 (a) and confined BL-WSe_2 (b). **c,d.** Cross-sectional TEM images of confined ML-WSe_2 (c) and BL-WSe_2 (d). **e.** Cross-sectional HAADF-STEM image of WSe_2/MoS_2 heterobilayer, overlain with the energy dispersive X-ray (EDX) spectra for Mo Kα (purple), S Kα (yellow), W Lα (grey) and Se Kα (green). Scale bars, 2 nm (c-e).

2.4 Material characterization

We characterized TMDs to verify material quality using Raman spectroscopy, photoluminescence (PL), and high-resolution transmission electron spectroscopy (HRTEM). Figure 9 shows Raman spectra, PL, and their mapping for confined monolayer (ML) and bilayer (BL) WSe_2. Raman mapping at the E^1_{2g} peak and PL mapping at 1.65 eV in Figure 9b,c confirms that the WSe_2 are selectively grown in trench area and monolayer.

As for confined bilayer WSe_2, on the other hand, broadened A_{1g} peak and appearance of B^1_{2g} peak of Raman spectra and red shift of PL spectra peak from 1.65 to 1.6 eV with reduced intensity verify its band transition from direct-gap to indirect-gap. Their mappings also verify that the confined bilayer WSe_2 is uniformly achieved.

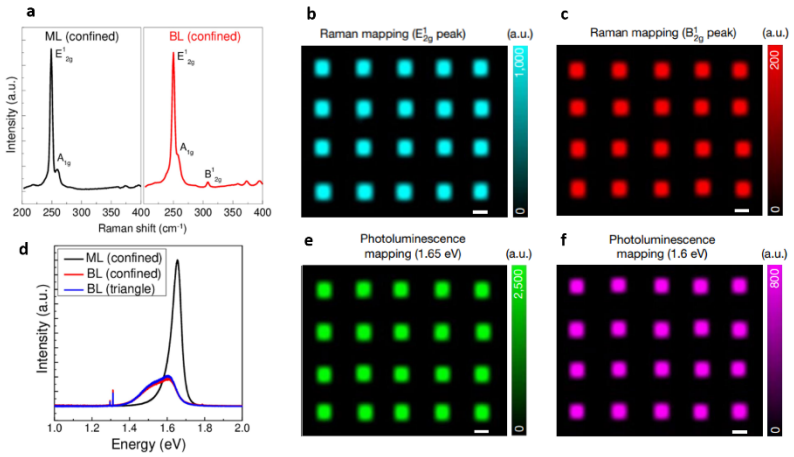

Figure 9. a,b. Raman spectra, **c-f.** Raman mapping and **g,h.** Cross sectional TEM images for confined ML-WSe_2 (a,c,d,g) and BL-WSe_2 (b,e,f,h).

We investigated full width at half-maximum (FWHM) of the PL spectrum at room temperature (300 K) to verify material quality (Figure 10). While the average FWHM of PL peak at 1.65 eV for multi-domain confined WSe_2 is approximately 85 meV, the average FWHM for single-domain confined WSe_2 is 55 meV, which is similar to that of high-quality single-crystalline WSe_2 flakes, and which is attributed to the lack of grain boundary for single-domain confined WSe_2[16,17].

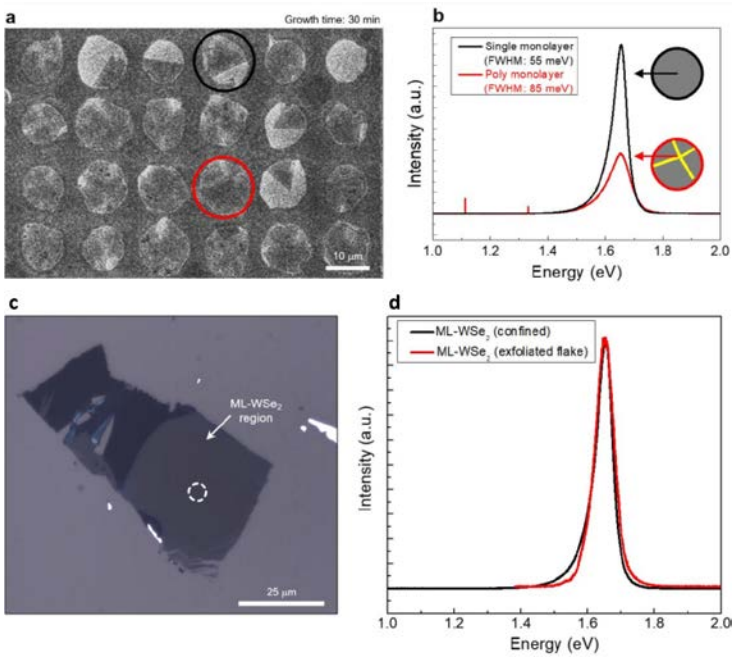

Figure 10. Comparison of confined single- and poly-ML-WSe_2. a,b. SEM morphology (a) and PL characteristics (b) of confined single- and poly-ML-WSe_2 in 10 μm-sized sapphire pockets. **c.** Optical microscopy (OM) image of an as-exfoliated ML-WSe_2 flake transferred onto SiO_2 substrate, wherein circular mark indicates laser-irradiated spot. **d.** PL spectra of confined ML-WSe_2 film (black) and as-exfoliated ML-WSe_2 flake (red), respectively.

We further investigated the material quality of confined mono- and bi-layer WSe_2 thoroughly with high-angle annular dark field scanning transmission electron microscopy (HAADF-STEM) and X-ray photoelectron spectroscopy (XPS). STEM images in Figure 11a,b show confined bilayer WSe_2 has no

obvious step bunching, distortions, or curling due to possible strain that can potentially arise at the edge of the a-SiO_2 trench, and thus confirm the uniformity of the bilayer WSe_2.

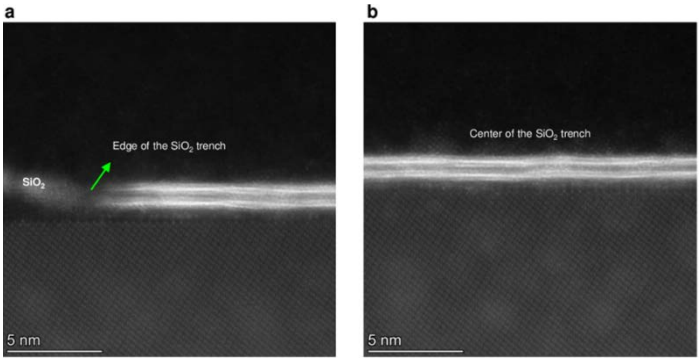

Figure 11. a,**b.** STEM images of confined bilayer WSe_2 grown at the edge (a) and center (b) of SiO_2 trench.

From plan-view STEM analysis shown in Figure 12, Se vacancy is observed as the dominant point defect with a density of less than 1% (~1.6×10^{13}/cm) and inset fast Fourier transform (FFT) pattern in Figure 12b indicates that bilayer WSe_2 is epitaxially aligned with AA' stacking. Measured atomic percentages of W 4*f* and Se 3*d* by XPS were 33.72% and 66.28%, respectively, verifying stoichiometric ratios, and the peak positions of W ($4f_{5/2}$ and $4f_{7/2}$) and Se ($3d_{3/2}$ and $3d_{5/2}$) were 34.8, 32.6, 55.7 and 55 eV, respectively, which matches well with pure single-crystalline WSe_2[18].

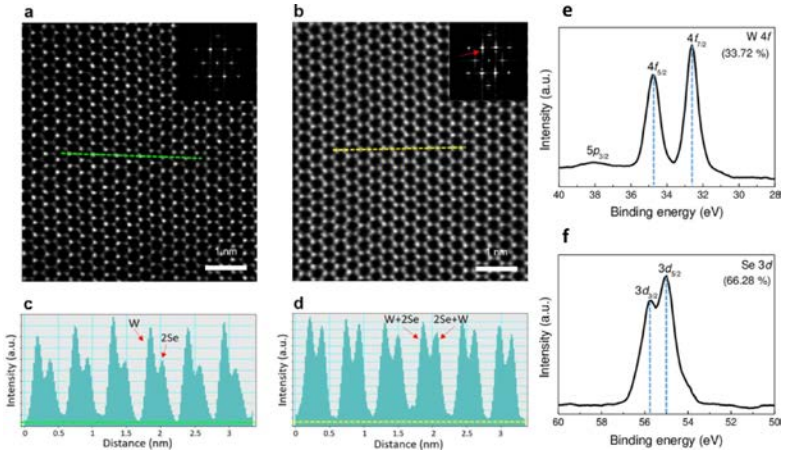

Figure 12. Plan-view HAADF-STEM and XPS analysis of confined WSe_2. a–d. Plan-view HAADF-STEM images of confined ML- (a) and BL-WSe_2 (b). The FFT pattern peak was split into two due to the coexistence of W and 2Se in the same atomic arrangement [red arrow in (**b**)]. Confined ML- and BL-WSe_2 were also compared by line intensity profiling (**c, d**) each extracted from green line in (**a**) and yellow line in (**b**). **e,f.** XPS data of confined ML-WSe_2.

Single domain MoS_2/WSe_2 heterostructure arrays were also characterized by Raman spectroscopy and XPS. Raman mapping was performed at MoS_2 E^1_{2g} peak (384.9cm^{-1}) and shows uniform MoS_2 layer on single domain ML-WSe_2 arrays (Figure 13a). Raman and PL spectrum in Figure 13 b,c confirms heterobilayer and slight peak shift from their original peak position verifies interlayer exciton coupling[19]. In addition, high crystalline quality of MoS_2 is confirmed by XPS spectra observed in narrow-scan data of Mo ($3d_{3/2}$ and $3_{d5/2}$) and S ($2p_{1/2}$ and $2p_{3/2}$), indicating no signs of defects or atomic mixing related to Mo^{6+} peak at ~236 eV[20].

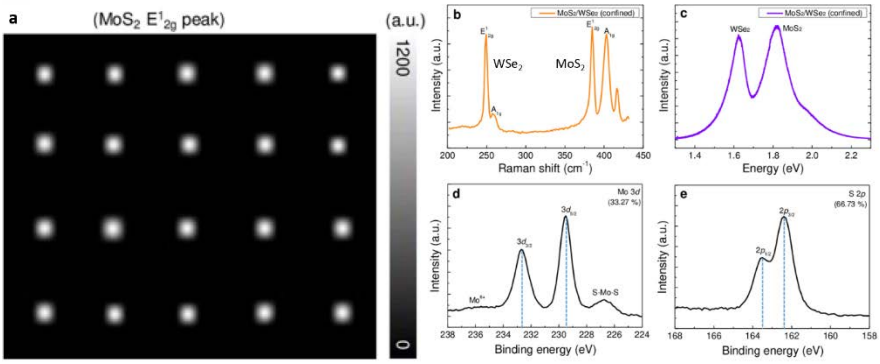

Figure 13. Confined MoS_2/WSe_2 heterobilayer. a–e. Raman mapping of the E^1_{2g} peak on the MoS_2/WSe_2 heterobilayer at each trench (a). Raman (b), PL (c) and XPS (d,e) spectra of MoS_2/Wse_2 heterobilayer.

2.5 Device performances

To verify the electrical performance of single-domain confined TMDs, we fabricated field effect transistor (FET) arrays on the ML- and BL-WSe_2 grown on a 2-inch wafer (Figure 14a). Figure 14b shows representative I_{ds}–V_{gs} characteristics measured from one of the BL-WSe_2 FET arrays. The FET exhibits an on/off current ratio of greater than 10^8, a subthreshold swing of 240.5 mV/dec, a maximum on-current (I_{on}) density of up to 155.8 μA/μm and a field-effect mobility ($\mu_{eff} = g_m L/WC_g V_{ds}$, C_g = 11.6 nF/cm^2, where g_m, L, W, and C_g are the transconductance, channel length, width, and gate capacitance, respectively) of up to 103.5 cm^2/Vs, at V_{ds} = -1 V. Furthermore, a saturation current of up to 465 μA/μm was observed via output characteristics (Figure 14c). We benchmarked the results of WSe_2 FETs reported so far and compared them to our devices (Figure 14d)[21–30]. We highlight that the electrical properties of FETs fabricated with confined ML-/BL-WSe_2 are comparable to the best properties reported for single-crystalline WSe_2-based FETs, and similar to (or better than) those of as-exfoliated flake-based ML-/BL-WSe_2 FETs (Figure 14e). We then performed statistical analysis on the FET arrays with respect to I_{on} per width and μ_{eff} (Figure 14f). The FETs exhibit a Gaussian distribution in both I_{on} per width and μ_{eff}; the average and variation values are 89.9 μA/μm and 17.3% for I_{on} density and 79.1 cm^2/Vs and 24.1% for μ_{eff}. Detailed statistical investigation with respect to I_{on} density, μ_{eff}, subthreshold swing, on/off current ratio and threshold voltage (V_{th}) on 213 FETs fabricated with confined BL-WSe_2 are provided in Figure 15 and 16 with an estimated yield of 93.9%.

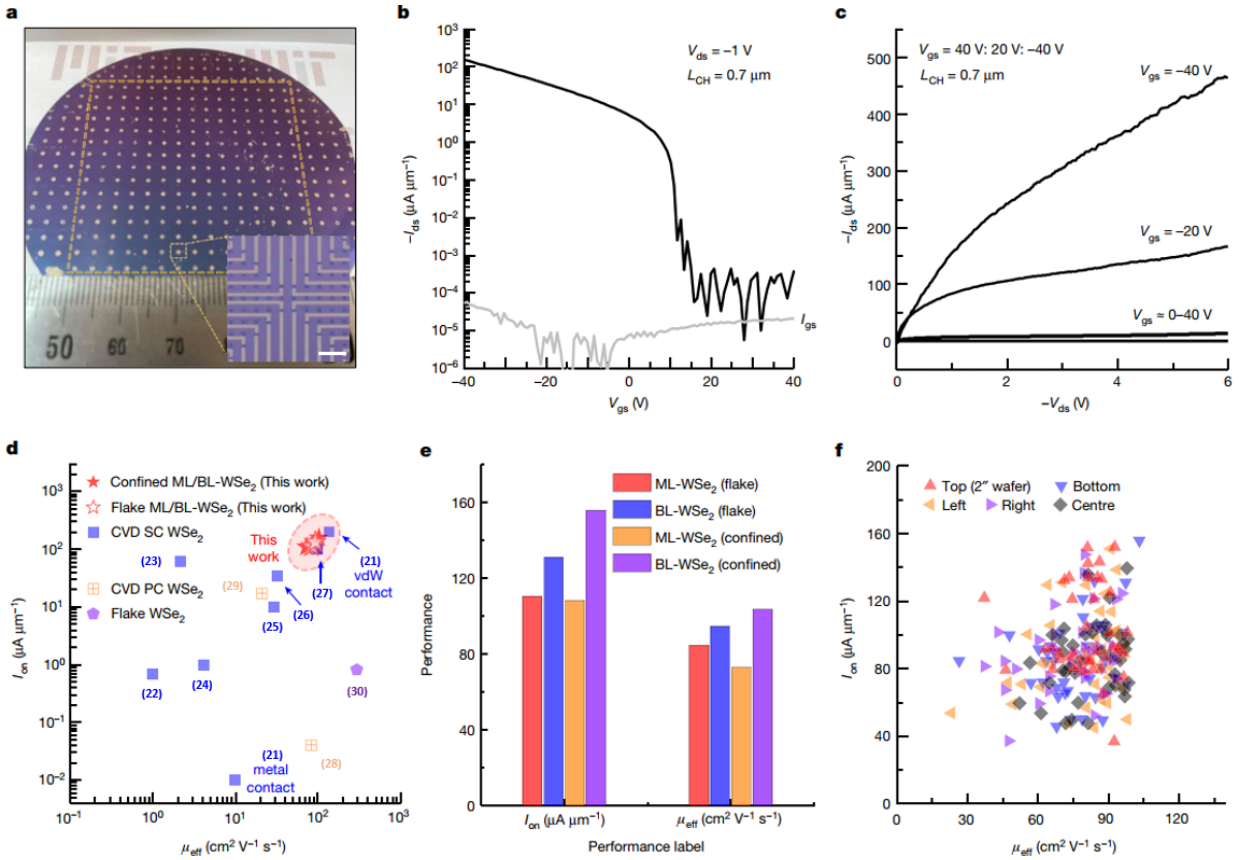

Figure 14. Electrical performance of confined WSe_2. a. Photograph of an integrated confined BL-WSe_2 FET arrays on an a-SiO_2/Si wafer with size 5.1 cm × 5.1 cm. Inset shows micrograph of an individual FET array, where 20 FETs are integrated. Scale bar, 10 μm. **b.** Transfer characteristics of confined BL-WSe_2 FET at V_{ds} = −1 V, where L_{CH} (channel length) is 0.7 μm. Obtained results show maximum on-current density of up to 155.8 μA/μm and a field-effect mobility of up to 103.5 cm^2/Vs. **c.** Output characteristics of confined BL-WSe_2 FET. **d.** Comparison of results with respect to I_{on} and μ_{eff} between FETs fabricated with as-exfoliated ML- and BL-WSe_2 flakes and confined ML- and BL-WSe_2 films. **e.** Statistical distribution with respect to I_{on} and μ_{eff} achieved at different positions from confined BL-WSe_2 FET arrays.

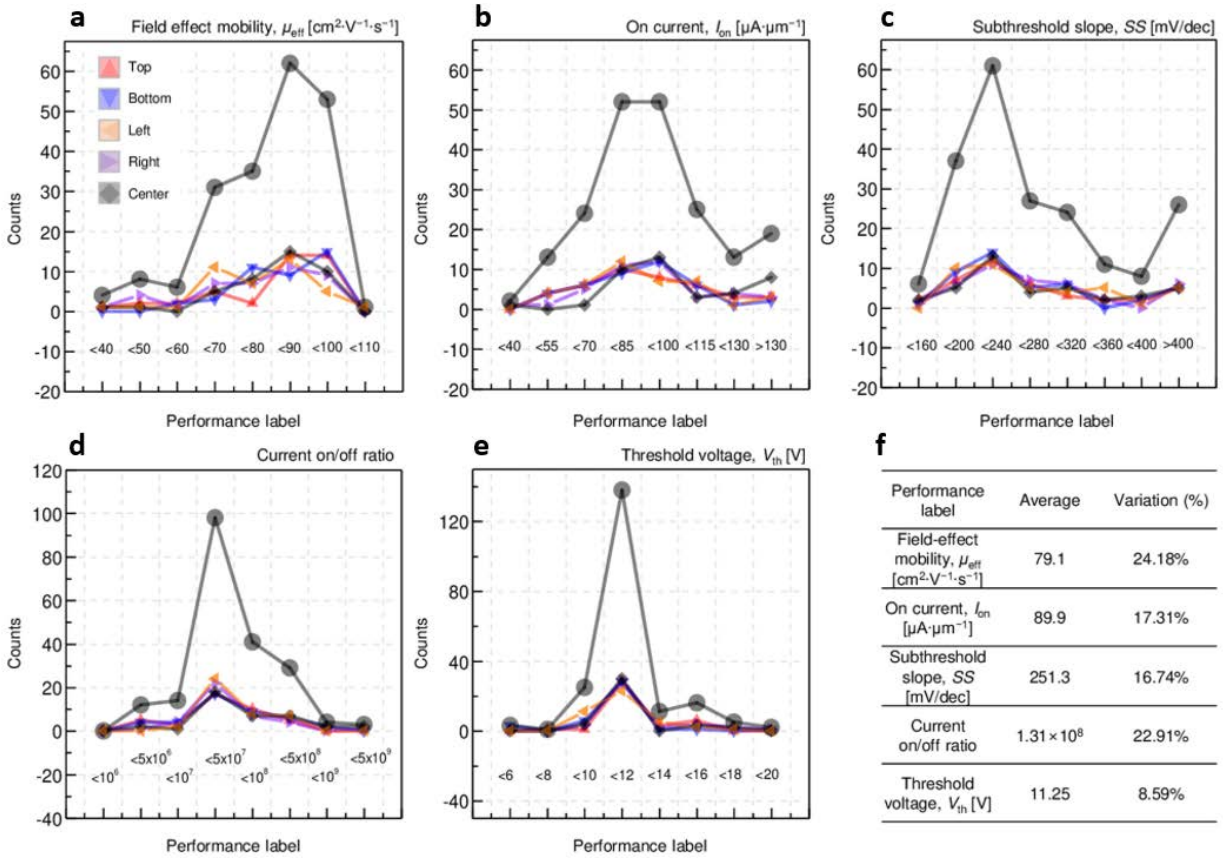

f

Performance label	Average	Variation (%)
Field-effect mobility, μ_{eff} [cm²·V⁻¹·s⁻¹]	79.1	24.18%
On current, I_{on} [μA·μm⁻¹]	89.9	17.31%
Subthreshold slope, *SS* [mV/dec]	251.3	16.74%
Current on/off ratio	1.31×10^8	22.91%
Threshold voltage, V_{th} [V]	11.25	8.59%

Figure 15. Yield estimation and statistical analysis on FETs fabricated with confined BL-WSe_2. a–e. Statistical analysis on 200 FETs fabricated with confined BL-WSe_2, where field-effect mobility (a), on current (b), subthreshold slope (c), current on/off ratio (d), and threshold voltage (e) were extracted and investigated. **f.** Summary table for performance labels.

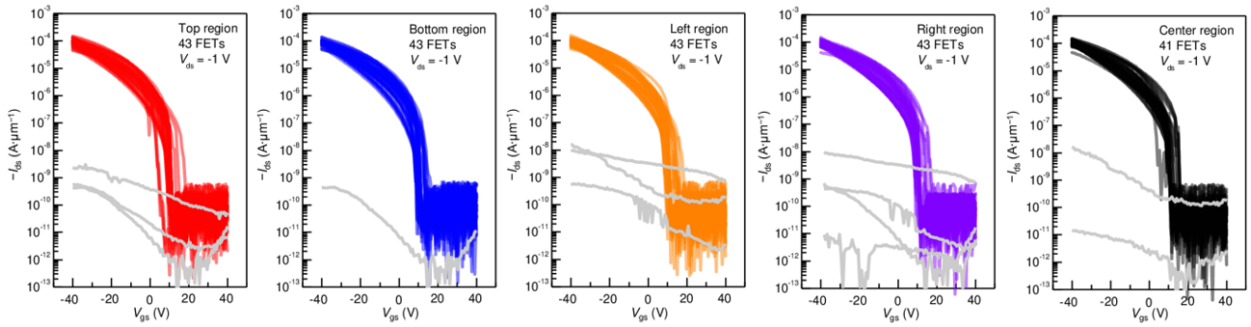

Figure 16. Transfer characteristics of confined BL-WSe_2 FETs. Each graph shows transfer characteristics for over 40 FETs; top region (red), bottom region (blue), left region (orange), right region (violet), and center region (black) of FET arrays fabricated on 2-inch wafer. Grey curves denote transfer characteristics of defective FETs.

We also investigated electrical characteristics of confined ML- and BL-MoS_2 on a-HfO_2 deposited Si/SiO_2 substrate to meet the requirement of industrialization in the logic and memory sectors, which requires single-crystalline TMDs formation on amorphous surfaces on Si wafers and single-crystalline heterostructures at the wafer scale. We fabricated the FETs on as-grown ML- and BL-MoS_2 on a-HfO_2/Si wafers without any transfer process and they showed excellent electrical characteristics. Figure 17b shows

I_{ds}–V_{ds} measured from fabricated ML- and BL-MoS_2 FETs. The FETs exhibit a maximum I_{on} density of up to 86.7 μA/μm (ML-MoS_2) and 129.3 μA/μm (BL-MoS_2), a μ_{eff} of up to 62.2 cm^2/Vs and 88.61 cm^2/Vs, wherein $C_{g,HfO2}$ = 600 nF/cm^2 and V_{ds} = 1 V. In addition, we next performed statistical analysis on the 42 MoS_2 FETs (21 ML-MoS_2 FETs and 21 BL-MoS_2 FETs) with respect to the I_{on} per width and μ_{eff}, wherein the average values of I_{on} and μ_{eff} are 71.4 μA/μm (for I_{on} per width of ML-MoS_2 FETs), 99.3 μA/μm (for I_{on} per width of BL-MoS_2 FETs), 51.2 cm^2/Vs (for μ_{eff} of ML-MoS_2 FETs), and 71.2 cm^2/Vs (for μ_{eff} of BL-MoS_2 FETs), respectively. Here, we estimate 23.8% and 25.2% of variation for I_{on} per width values of ML- and BL-MoS_2 FETs, and 20.3% and 24.9% of variation for μ_{eff} values of ML- and BL-MoS_2 FETs, respectively, with a 90.5% device yield (Figure 17c).

We characterize valleytronic performance as well with MoS_2/WSe_2 heterobilayer arrays. We investigated valley-polarized carrier dynamics of the heterobilayer arrays via ultrafast circular dichroism based on time-resolved pump–probe spectroscopy (Figure 17d). We measured valley lifetime from our single-domain MoS_2/WSe_2 arrays (approximately hundreds of picoseconds at 300 K and a few nanoseconds at 77 K).

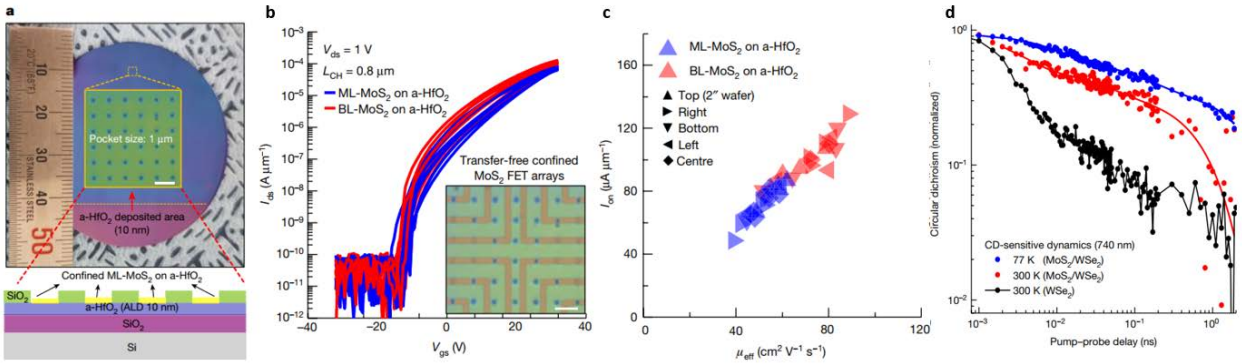

Figure 17. Confined TMD growth on a-HfO_2 deposited on an Si wafer and valley-polarized interlayer excitations in ML-WSe_2 and heterobilayer (MoS_2/WSe_2). a. Photograph and schematic image of a-HfO_2 deposited by atomic layer deposition (ALD) system on an Si wafer in a reduced trench size (1 μm). **b.** Transfer characteristics of FETs fabricated with confined ML- and BL-MoS_2 on an a-HfO_2 coated Si substrate. Inset denotes optical microscopic (OM) image of confined MoS_2 FET arrays fabricated on a-HfO_2. **c.** Statistical distribution with respect to I_{on} per width and μ_{eff} achieved from confined ML- and BL-MoS_2 FET arrays. **d.** Time-resolved circular dichroism (CD) response in ML-WSe_2 at 300 K (black) and heterobilayer (MoS_2/WSe_2) at 300 K and 77 K, where the red and blue solid lines are the cumulative fits.

Chapter 3

Conclusions

In conclusion, we have demonstrated the synthesis of single-domain arrays of 2D TMDs at the wafer scale using a confined-growth technique. This growth technique enables layer-by-layer synthesis with critical Gibbs free energy difference, realizing wafer-scale single-domain homobilayers and heterobilayers on arbitrary substrates. In addition, our confined TMD layers show excellent electrical performance, comparable to that of flake TMDs.

Therefore, our confined-growth technique can not only overcome the difficulty in controlling the kinetics of 2D materials at the wafer scale, which has been a major obstacle for 2D TMDs, but also show great potential for creating various single-crystalline van der Waals integration at a large scale, providing a route for building a 2D-material-based electronics platform.

Appendix A: Experimental Methods

DFT calculation for selective confined growth of TMDs

DFT calculations were performed using the Vienna ab initio Simulation Package (VASP) which uses projector augmented wave pseudopotentials[31] and a plane-wave basis set[32]. Generalized gradient approximation of Perdew-Burke-Ernzerhof (PBE) functional was used to describe the electronic exchange-correlation interaction[33]. The valence electron configurations of W, Se, O, Al and Si are $6s^2 5d^4$, $4s^2 4p^4$, $2s^2 2p^4$, $3s^2 3p^1$ and $3s^2 3p^2$, respectively. The energy cut-off for plane-wave expansion was set at 420 eV. Because large cells (lattice constant > 10 Å) were used for calculation, the Brillouin zone was sampled by using Γ-point only *k*-point grid. The surface binding interaction was investigated by placing the WO_3, Se and WSe_2 clusters on top of the a-HfO_2, Al_2O_3 (0001) and a-SiO_2 slab, respectively. a-HfO_2, a-SiO_2 and *c*-plane Al_2O_3 surfaces were passivated by H atoms to mimic the Ar/H_2 ambient growth environment. The amorphous HfO_2 and SiO_2 atomic structure was obtained by subjecting their crystalline structure to a melt–quench process simulated by ab initio molecular dynamics[34]. Structures were optimized by relaxing top adsorbent atoms with substrate atoms fixed. The criterion for structure relaxation is that the force exerted on each atom should be less than 0.01 eV/Å. Electronic minimization is reached when the system energy difference between two consecutive iterations is smaller than 10^{-5} eV. The surface binding energy for adsorbent A on substrate B is calculated as $E_b = E_{A/B} - E_A - E_B$ where $E_{A/B}$, E_A and E_B are the energies of the adsorbing system A/B, isolated adsorbent A and substrate B, respectively.

Confined pattern fabrication

For confined growth of TMDs, we coated LOR 3A and photoresist (S1805) on a sapphire substrate and patterned it with an AS200 i-line stepper (AutoStep 200). A ~25-nm-thick a-SiO_2 was deposited on a photoresist (PR)-patterned sapphire substrate with an electron-beam evaporator. Then, to fabricate sapphire pockets, the a-SiO2 pattern was lifted off with Remover PG (Kayaku Advanced Materials) and rinsed in acetone and isopropanol for 15 min each.

Synthesis of WSe_2 and MoS_2

Confined TMDs were synthesized in a quartz tube with 4-inch diameter. 300 mg of Se or S powders for (zone I), and 30 mg of WO_3 or MoO_3 powders for (zone II) were placed, and the distance between them was fixed at 33 cm. The sapphire substrate patterned with a-SiO_2 was vertically loaded 6 cm behind the WO_3 or MoO_3 powders, and the front and back of the substrate were covered with quartz plates to minimize direct reaction. Before synthesizing confined ML-WSe_2, the air in the quartz tube was removed with a vacuum pump. After closing the vacuum valve, a ratio of Ar (50 sccm)/H_2 (50 sccm) was used as the carrier gas to fill the tube before opening the atmospheric valve. The ratio of Ar/H_2 was maintained constantly. The growth temperatures of zones I and II were obtained by heating at ramp rates of 15 °C/min and 30 °C/min, respectively, then held at 450 °C (zone I) and 890 °C (zone II) for 10 min before naturally cooling down to room temperature. For the confined BL-WSe_2, a second WSe_2 layer synthesis was performed with carrier gas having a ratio of Ar (35 sccm)/H_2 (65 sccm). For the confined heterostructure (MoS_2/WSe_2), MoS_2 synthesis was performed at 200 °C (zone I) and 750 °C (zone II) with ramp rates of 8 °C/min and 30 °C/min, respectively. In particular, to improve the growth selectivity on the a-HfO_2

substrate, we reduced the size of the a-SiO_2 trenches to 1 μm and increased the overall flow rate of Ar/H_2 from 100 sccm (Ar (50 sccm)/H_2 (50 sccm)) to 200 sccm (Ar (100 sccm)/H_2 (100 sccm)). All reactions were performed at atmospheric pressure, and all TMD powders were from Sigma-Aldrich with purity of more than 99.99%. We emphasize that it is important that various parameters must be kept consistent for growth reproducibility of confined TMDs.

Characterization of confined TMDs

Raman and photoluminescence spectra were measured using a Renishaw InVia Reflex micro-spectrometer with 532-nm laser. The light was dispersed by a holographic grating with 2,400 grooves/mm. For Raman and photoluminescence mapping images, samples were scanned on an *x*–*y* piezo stage with laser illumination. Scanning electron microscope (SEM) images were measured with an in-Lens detector using a high-resolution SEM (ZEISS Merlin). The working distance was 6 mm at an accelerating voltage of 2 kV and a probe current of 70 pA. Transmission electron microscopy (TEM) characterization was performed using a JEOL JEM-2100F with an accelerating voltage of 200 kV and STEM (Titan Themis Z G3 Cs-Corrected) with an accelerating voltage of 60 kV. Energy dispersive X-ray (EDX) line profiles were taken with the Velox software in STEM mode using the characteristic Mo Kα, S Kα, W Lα and Se Kα X-ray signals. XPS spectra are measured with a magnesium Kα source (MultiLab 2000, Thermo VG), and the peak energies were calibrated by the C 1*s* peak at 284.8 eV. AFM morphology analysis was performed using an XE 100 (Park Systems).

Device fabrication and electrical measurements

For device fabrication using confined ML-/BL-WSe_2, a 600-nm-thick Au film was deposited on confined WSe_2/sapphire by electron-beam evaporation. The Au/WSe_2 stack was peeled off using a thermal release tape as a handling layer and transferred onto a 300-nm-thick SiO_2/heavily p-doped silicon wafer. The thermal release tape was removed on a hot plate at 120 °C, followed by oxygen plasma treatment to remove tape residues from the Au film. Then, the Au film was etched with Au etchant and rinsed with deionized water (to compare the electrical characteristics, a few-layer WSe_2 flake was also transferred in the same way). After the transfer of confined ML-/BL-WSe_2 on a-SiO_2 substrate, align marks for electron-beam lithography (EBL) process were patterned on an a-SiO_2 substrate using an optical lithography process, followed by the deposition of 2.5-nm-thick Ti and 7.5-nm-thick Au using an electron-beam evaporator. Then, drain and source contact regions with a width of 2 μm were patterned using an EBL process. For EBL photoresists, polymethyl methacrylate (PMMA) A4 and PMMA A6 were spin-coated at 3,000 rpm and baked at 180 °C for 150 s. After developing the PMMA, 10-nm-thick Pt and 80-nm-thick Au layers were deposited using an electron-beam evaporator. Finally, the areas, except the source/drain contact metal regions, were removed by a lift-off process. For device fabrication using confined ML-/BL-MoS_2 on a-HfO_2, the same processes from patterning align marks for EBL process to developing the PMMA were performed. Then 10-nm-thick Ni and 80-nm-thick Au layers were deposited using an electron-beam evaporator, followed by a lift-off process. Here we emphasize that we directly fabricated confined ML-/BL-MoS_2 FETs on a-HfO_2-deposited Si wafers without a transfer process. The current–voltage characteristics were measured with an Agilent B2900A. All measurements were conducted at room temperature in the air. In addition, 2-inch confined BL-WSe_2 was transferred onto 300-nm-thick SiO_2/Si substrate with a size of 5.1 × 5.1 cm^2. Kelvin probe force microscopy (KPFM) confirmed highly uniform distribution of work functions (5.08 eV) on confined BL-WSe_2 (Figure 18).

Source and drain electrodes with a channel length (*L*CH) of 0.7 μm were then integrated using platinum; a hole barrier height of 0.31 eV was estimated via modified Richardson plotting (Figure 19)[35].

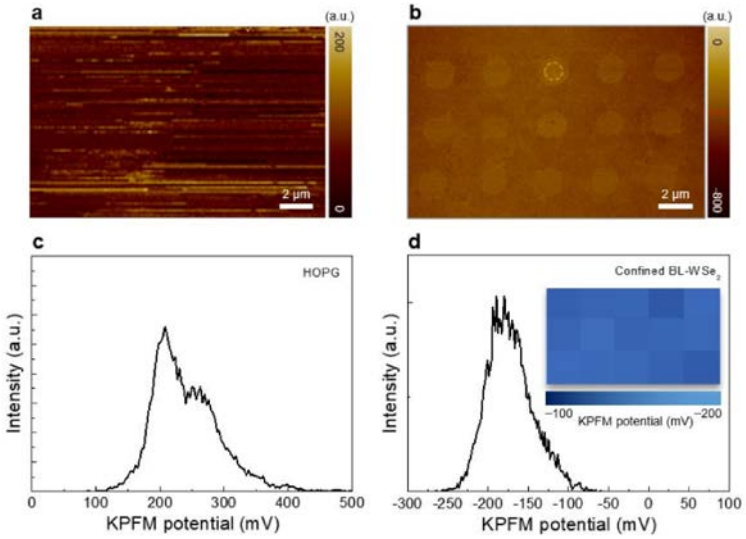

Figure 18. KPFM analysis on confined BL-WSe_2. a,b. KPFM mapping image of HOPG sample (a) and confined BL-WSe_2 (b). **c,d.** KPFM potential profile of HOPG sample (c) and confined BL-WSe2 (d). Here, inset color map shows KPFM potential distribution observed in confined BL-WSe_2 depicted in (b).

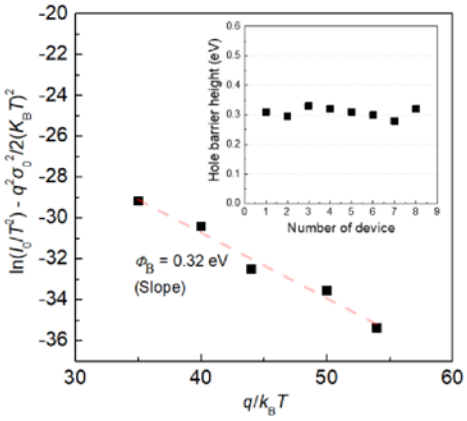

Figure 19. Modified Richardson plot method for extracting hole barrier height. Inset shows hole barrier height distribution extracted from 8 FETs.

Time-resolved pump–probe spectroscopy

To investigate valley-polarized carrier dynamics, we have measured ultrafast circular dichroism (CD) based on time-resolved pump–probe spectroscopy. A 100-kHz Yb-based regenerative amplifier system (Light Conversion PHAROS) provided a femtosecond laser pulse, and a sequential optical parametric amplifier (ORPHEUS) served wavelength-tunable pump and probe pulses resonant with A-exciton resonance of WSe_2 with pulse duration of 50 fs and spectral bandwidth of 50 meV. Samples on cryostat have been illuminated by a pump excitation pulse using a 40x objective lens. Pump-induced changes in probe reflectance have been recorded as a function of time delay given by a mechanical

translational stage and lock-in amplifier. The polarization profiles of pump and probe pulses are individually controlled by a pair consisting of a half-wave plate and a quarter-wave plate. We have measured the signal when the pump and probe pulses exhibit the same helicity of circular polarization (co-polarized), and opposite helicity of the polarization (cross-polarized). Valley-dependent ultrafast CD responses shown in Figure 17d were acquired by the differences between co-polarized and cross-polarized pump–probe responses. Experimental details can be found in the previous work[36].

Appendix B: Theoretical calculations

Confined single domain arrays growth mechanism of TMDs

Classical nucleation and growth theory states that materials growth on a substrate involves nucleation and growth processes. In our confined growth experiment of WSe_2, the formed WSe_2 clusters are first adsorbed onto the growth substrate and nucleate into small particles. The formed nucleation will then grow larger by continuously absorbing newly formed WSe_2 clusters. Therefore, one important factor that influences the nucleation and growth rate is the binding energy of WSe_2 clusters on the growth substrate. Thus, we calculated the binding energies of precursors W_3O_9 and Se_2 and product W_3Se_6 clusters on c-Al_2O_3 and a-SiO_2 substrates to find two materials with different critical Gibbs free energies. When using the CVD method with WO_3 and Se as precursors, there are two possible reaction mechanisms that can lead to WSe_2 growth[37]. The first mechanism is the on-substrate reaction (as shown in Figure 1c). Volatile WO_3 (or reduced WO_3-xSe_x) evaporates and is deposited on the desired substrate, followed by selenium reduction and conversion into WSe_2. The second mechanism is the gas phase reaction. WO_3 and Se only react in the gas phase, in which the formed WSe_2 cluster diffuses onto the growth substrate for nucleation and growth. In terms of gas phase reaction, we have calculated the energetics of the following reactions:

$$W_3O_9 + 5.25Se_2 \rightarrow W_3Se_6 + 4.5SeO_2,\ \Delta G = 9.057\ eV\ (1)$$
$$W_3O_9 + 4.5Se_2 + 3H_2 \rightarrow W_3Se_6 + 3SeO_2 + 3H_2O,\ \Delta G = 4.644\ eV\ (2)$$
$$W_3O_9 + 3Se_2 + 9H_2 \rightarrow W_3Se_6 + 9H_2O,\ \Delta G = -4.181\ eV\ (3)$$
$$W_3O_9 + 9H_2 \rightarrow W_3 + 9H_2O,\ \Delta G = -4.181\ eV\ (4)$$

We can see that the Se reduction of WO_3 is only possible with the presence of H_2. This result is consistent with previous reports[38,39] and with our experimental observations. The negative Gibbs free energy change in reaction (3) suggests that gas phase reaction is involved and contributes to the CVD WSe_2 growth. The WSe_2 cluster formed in a gas phase is preferentially deposited onto c-Al_2O_3 and a-HfO_2 substrates due to stronger binding energy.

Growth methods for reproducibility of confined TMDs

For uniformity and reproducibility of confined TMDs, various parameters must be kept consistent. i) Since the selective growth of confined TMDs is carried out under atmospheric pressure, the air in the quartz tube must be completely removed with a vacuum pump and then filled with carrier gases (Ar/H2) to sufficiently saturate the quartz tube. In addition, the connection part should be tightened as much as possible so that external air does not flow into the quartz tube during the growth process. ii) The external pressure/temperature must be kept constant. Minor changes can affect gas flow and increase/decrease temperature during growth. iii) In the process of preparing samples and TMDs powder, one should be careful of external contamination sources as it can change the gas phase reaction during the synthesis process.

Characterization of device

To estimate the work function of confined BL-WSe_2, scanning probe microscopy measurements were performed in the non-contact Kelvin probe force microscopy (KPFM) modes using an NX10 system (Park Systems Corp.). KPFM measurements were performed under dark and ambient conditions using a platinum/iridium (Pt/Ir)-coated Si tip. In the KPFM measurements, the surface work function of the sample (Φ_{sample}) was obtained using the following equations:

$$\Phi_{sample} = eV_{CPD1} - eV_{CPD2} + \Phi_{HOPG},$$
$$V_{CPD1} = V_{CPD\_tip} - V_{CPD\_sample},$$
$$V_{CPD2} = V_{CPD\_tip} - V_{CPD\_HOPG},$$
$$\Phi_{sample} = e(V_{HOPG} - V_{sample}) + \Phi_{HOPG}.$$

Here, V_{CPD1} is the contact potential difference (CPD) between the tip and the sample, and V_{CPD2} is CPD between the tip and the highly oriented pyrolytic graphite (HOPG), respectively. Φ_{HOPG} denotes the work function of HOPG; the HOPG is conventionally used to calibrate the work function of the KPFM tip because it has a clean surface, and its work function is well known to be 4.6 eV[40]. To determine the Schottky barrier height between Pt source/drain electrodes and confined BL-WSe2, the electrical characterization with respect to temperature was performed with an Agilent 4155C under vacuum. Then, a thermionic emission current equation for a Pt-WSe_2-Pt junction was used as follows:

$$I_0 = AA^{**}T^2 \exp\left(\frac{-q\Phi_B}{k_B T}\right)\left[\exp\left(\frac{qV_{DS}}{nk_B T}\right) - 1\right],$$

Where I_0 is the saturation current, A is the effective area, A^{**} is the Richardson constant, T is the temperature in Kelvin, q is the elementary charge, Φ_B is the Schottky barrier height, k_B is the Boltzmann constant, V_{DS} is the voltage across the source and drain, and n is the ideality factor. When a reverse bias is applied, the exp (qV_{DS}/nk_BT) term becomes ignorable and the above equation can be simplified as follows:

$$I_0 = -AA^{**}T^2 \exp\left(\frac{-q\Phi_B}{k_B T}\right) .$$

Moving the T^2 term to the left-hand side of the equation and taking the natural log on both sides, the following equation was obtained:

$$\ln\left(\frac{I_0}{T^2}\right) = \ln\left(AA^{**}\right) - \frac{q\Phi_B}{k_B T} .$$

Because WSe_2 FET operates under thermionic emission and diffusion mechanisms, a conventional Richardson plot does not give a linear fit over the entire temperature range. Thus, we employed a

modified Richardson plotting method based on a thermionic emission-diffusion model[41]. The linearity in the $\ln(I_0/T^2) - q^2\sigma_0{}^2/2(k_BT)^2$ versus q/k_BT plot was obtained, where σ_0 is the standard deviation of the Gaussian distribution. From the slope in the modified Richardson plot, the hole barrier height was estimated (Figure 19).

References

1. Novoselov, Kostya S., et al. "Electric field effect in atomically thin carbon films." *science* 306.5696 (2004): 666-669.
2. Das, Santanu, et al. "Synthesis, properties, and applications of 2-D materials: A comprehensive review." *Critical Reviews in Solid State and Materials Sciences* 39.4 (2014): 231-252.
3. Geim, Andre K., and Irina V. Grigorieva. "Van der Waals heterostructures." *Nature* 499.7459 (2013): 419-425.
4. Shim, Jaewoo, et al. "Controlled crack propagation for atomic precision handling of wafer-scale two-dimensional materials." *Science* 362.6415 (2018): 665-670.
5. Iannaccone, Giuseppe, et al. "Quantum engineering of transistors based on 2D materials heterostructures." *Nature nanotechnology* 13.3 (2018): 183-191.
6. Molaei, Mohammad Jafar, Mohammad Younas, and Mashallah Rezakazemi. "Van der Waals heterostructures in ultrathin 2D solar cells: State-of-the-art review." *Materials Science and Engineering: B* 285 (2022): 115936.
7. Long, Mingsheng, et al. "Progress, challenges, and opportunities for 2D material based photodetectors." *Advanced Functional Materials* 29.19 (2019): 1803807.
8. Withers, Freddie, et al. "Light-emitting diodes by band-structure engineering in van der Waals heterostructures." *Nature materials* 14.3 (2015): 301-306.
9. Schaibley, John R., et al. "Valleytronics in 2D materials." *Nature Reviews Materials* 1.11 (2016): 1-15.
10. Sierra, Juan F., et al. "Van der Waals heterostructures for spintronics and opto-spintronics." *Nature Nanotechnology* 16.8 (2021): 856-868.
11. Niu, Wen-Jun, et al. "Opportunities and challenges in precise synthesis of transition metal single-atom supported by 2D materials as catalysts toward oxygen reduction reaction." *Advanced Functional Materials* 31.35 (2021): 2103558.
12. Pomerantseva, Ekaterina, and Yury Gogotsi. "Two-dimensional heterostructures for energy storage." *Nature Energy* 2.7 (2017): 1-6.
13. Li, T. et al. Epitaxial growth of wafer-scale molybdenum disulfide semiconductor single crystals on sapphire. Nat. Nanotechnol. 16, 1201–1207 (2021).
14. Li, J. et al. General synthesis of two-dimensional van der Waals heterostructure arrays. Nature 579, 368–374 (2020).
15. Kim, Ki Seok, et al. "Non-epitaxial single-crystal 2D material growth by geometric confinement." *Nature* (2023): 1-7.
16. Rivera, P. et al. Observation of long-lived interlayer excitons in monolayer $MoSe_2$–WSe_2 heterostructures. Nat. Commun. 6, 6242 (2015).
17. Cadiz, F. et al. Excitonic linewidth approaching the homogeneous limit in MoS_2-based van der Waals heterostructures. Phys. Rev. X 7, 021026 (2017).
18. Zhang, R. et al. Controlled layer thinning and p-type doping of WSe2 by vapor XeF2. Adv. Funct. Mater. 27, 1702455 (2017).
19. Lin, Y. C. et al. Atomically thin resonant tunnel diodes built from synthetic van der Waals heterostructures. Nat. Commun. 6, 7311 (2015)
20. Kim, K. S. et al. Ultrasensitive MoS2 photodetector by serial nano-bridge multiheterojunction. Nat. Commun. 10, 4701 (2019).

21. Li, J. et al. General synthesis of two-dimensional van der Waals heterostructure arrays. Nature 579, 368–374 (2020).
22. Kozhakhmetov, A. et al. Scalable substitutional re-doping and its impact on the optical and electronic properties of tungsten diselenide. Adv. Mater. 32, 2005159 (2020).
23. Park, K. et al. Uniform, large-area self-limiting layer synthesis of tungsten diselenide. 2D Mater. 3, 014004 (2016).
24. Zhang, X. et al. Defect-controlled nucleation and orientation of WSe2 on hBN: a route to single-crystal epitaxial monolayers. ACS Nano 13, 3341–3352 (2019).
25. Lin, Y.-C. et al. Realizing large-scale, electronic-grade two-dimensional semiconductors. ACS Nano 12, 965–975 (2018).
26. Wang, X. et al. High-performance n-type transistors based on CVD-grown large-domain trilayer WSe2. APL Mater. 9, 071109 (2021).
27. Zhou, H. et al. Large area growth and electrical properties of p-type WSe2 atomic layers. Nano Lett. 15, 709–713 (2015).
28. Liu, B. et al. High-performance WSe2 field-effect transistors via controlled formation of in-plane heterojunctions. ACS Nano 10, 5153–5160 (2016).
29. Chen, M. et al. Gold-vapor-assisted chemical vapor deposition of aligned monolayer WSe2 with large domain size and fast growth rate. Nano Res. 13, 2625–2631 (2020)
30. Kim, W. et al. Field-dependent electrical and thermal transport in polycrystalline WSe2. Adv. Mater. Interfaces 5, 1701161 (2018).
31. Blöchl, P. E. Projector augmented-wave method. Phys. Rev. B 50, 17953 (1994).
32. Kresse, G. & Furthmüller, J. Efficient iterative schemes for ab initio total-energy calculations using a plane-wave basis set. Phys. Rev. B 54, 11169 (1996).
33. Perdew, J. P., Kieron, B. & Matthias, E. Generalized gradient approximation made simple. Phys. Rev. Lett. 77, 3865 (1996).
34. Buchholz, D. B. et al. The structure and properties of amorphous indium oxide. Chem. Mater. 26, 5401–5411 (2014).
35. Lin, Y.-F. et al. Barrier inhomogeneities at vertically stacked graphene-based heterostructures. Nanoscale 6, 795–799 (2014).
36. Jin, G. et al. Heteroepitaxial van der Waals semiconductor superlattices. Nat. Nanotechnol. 16, 1092–1098 (2021).
37. Zhou, D. et al. Unveiling the growth mechanism of MoS2 with chemical vapor deposition: from two-dimensional planar nucleation to self-seeding nucleation. Cryst. Growth Des 18, 1012–1019 (2018).
38. Huang, J. K. et al. Large-area synthesis of highly crystalline WSe2 monolayers and device applications. ACS Nano 8, 923–930 (2014).
39. Tsirlina, T. et al. Synthesis and characterization of inorganic fullerene-like WSe2 material. Fullerene Sci. Technol. 6, 157–165 (1998).
40. Jin, G. et al. Heteroepitaxial van der Waals semiconductor superlattices. Nat. Nanotechnol. 16, 1092–1098 (2021).
41. Lin, Y.-F. et al. Barrier inhomogeneities at vertically stacked graphene-based heterostructures. Nanoscale 6, 795-799 (2014).